Available online at www.sciencedirect.com
ScienceDirect
Journal of Hydrodynamics
2014,26(4):594-607
DOI: 10.1016/S1001-6058(14)60067-6
www.sciencedirect.com/science/journal/l0016058

A fully-explicit discontinuous Galerkin hydrodynamic model for variably-saturated porous media*

De MAET T., HANERT E.
Earth and Life Institute, Environmental Sciences, Université catholique de Louvain, B-1348 Louvain-la-Neuve, Belgium
Georges Lemaître Centre for Earth and Climate Research, Université catholique de Louvain, B-1348 Louvain-la-Neuve, Belgium, E-mail: thomas.demaet@uclouvain.be
VANCLOOSTER M.
Earth and Life Institute, Environmental Sciences, Université catholique de Louvain, B-1348 Louvain-la-Neuve, Belgium

(Received April 23, 2014, Revised June 10, 2014)

Abstract: Groundwater flows play a key role in the recharge of aquifers, the transport of solutes through subsurface systems or the control of surface runoff. Predicting these processes requires the use of groundwater models with their applicability directly linked to their accuracy and computational efficiency. In this paper, we present a new method to model water dynamics in variably- saturated porous media. Our model is based on a fully-explicit discontinuous-Galerkin formulation of the 3D Richards equation, which shows a perfect scaling on parallel architectures. We make use of an adapted jump penalty term for the discontinuous-Galerkin scheme and of a slope limiter algorithm to produce oscillation-free exactly conservative solutions. We show that such an approach is particularly well suited to infiltration fronts. The model results are in good agreement with the reference model Hydrus-1D and seem promising for large scale applications involving a coarse representation of saturated soil.

Key words: 3D subsurface flow model, discontinuous Galerkin method, slope limiters, explicit time integration

Introduction

A good understanding of subsurface water dynamics is essential in many hydrological, environmental and engineering applications. However, predicting such dynamics is still a difficult task. The difficulty mainly comes from the heterogeneity of the soil properties, the nonlinearity of the flow process and the absence of fast techniques to measure the hydraulic properties everywhere, at the appropriate scale. Given these issues, modeling the water flow in heterogeneous and often partially saturated porous media quickly and robustly is still a challenge.

By using a continuum approach, the water flow in variably saturated heterogeneous porous media can be modeled with the Richards equation (RE). This equation concerns both the water saturated zone (SZ) and the unsaturated zone (UZ). In the former, the equation models an incompressible fluid, leading to a constant water content θ. The pressure head h then reacts instantaneously to the boundary conditions. In the latter, the equation represents capillary physics and is complemented with the so-called retention-curve equation, which links the two variables. It is usual to refer to the θ-form and the h-form of the RE for the equations obtained by incorporating the retention curve in the conservation law to keep either θ or h as the sole model variable, respectively. On the one hand, the θ-form is not valid in the SZ, but is known to be more efficient in the UZ. On the other hand, the h-form is valid everywhere, although it is not mass conservative once discretized in time. The issues associated with the θ- and h-forms are usually overcome by combining both variables into a mixed formulation. When only the SZ is considered, the RE reduces to the groundwater equation that has its own numerical issues such as those associated with the

* **Biography:** De NATE T. (1986-), Male, Ph. D. Candidate

treatment of the free surface[1,2].

Despite the abundance of subsurface-flow models, the development of efficient and accurate discretizations of the RE is still an active field of research. The presence of two very different dynamics (in the SZ and UZ) leads to strong nonlinearity in the constitutive relations and then in the coupling between parabolic and elliptic partial differential equations. Implicit schemes have difficulties to handle such nonlinearities resulting in a lack of convergence[3]. Moreover, as the system dynamics can be highly transient, adaptive time steps are often mandatory[4]. In infiltration cases, this results in very small time steps, well below what is needed to reach a sufficient level of accuracy. As a result, the efficiency of implicit models for the RE is generally sub-optimal when infiltration fronts occur.

The efficiency of implicit models is further impaired by their poor scaling on parallel architectures. The current trend in computer designs is indeed to increase the performances relying on parallel architectures instead of enhancing the computational power of each processor individually. Current subsurface flow models therefore have to take advantage of parallelism, and some steps in that direction have been made with ParFlow[5,6], ParSWMS[7,8] and DuMu^x[9]. These models however only achieve sub-optimal scaling for the RE, except for some fully unsaturated test cases[8]. This is due to the use of implicit solvers as they require a large amount of communication between computational nodes to solve linear systems. Unlike implicit solvers, explicit solvers require only one exchange of information between nodes per time step. As implementing an explicit solver is simple, one can easily achieve a super-linear scaling, i.e., a scaling better than 100%, thanks to the additional computer caches coming from additional resources. Moreover, explicit solvers do not require any global matrix linear solver or the computation of a Jacobian, which are complex and costly.

In this paper, we present a 3D model of RE based on the discontinuous Galerkin (DG) finite element method (FEM) and an explicit time integration scheme. The model relies on slope limiters to locally ensure the monotonicity of the solution. It scales optimally at least up to 64 processors. A special treatment on the interface term between elements allows the existence of physical discontinuities in the water content between different types of soils. The model is mass-conservative at the machine precision. In the next two sections we present the mathematical formulation of the model and the explicit DGFEM discretization. In the fourth section, we present 1D and 3D numerical results, which focus on different physical and numerical aspects of groundwater flows.

1. Mathematical formulation

The RE is obtained by embedding Darcy's law into a mass conservation equation:

$$\frac{\partial \theta}{\partial t} = \nabla \cdot (\boldsymbol{K} \cdot \nabla (h + z)) + s \tag{1}$$

$$\theta = f_\theta(h) \tag{2}$$

where θ is the volumetric soil water content, h the pressure head, z the depth, s a sink-source term, $\boldsymbol{K}$ the water conductivity tensor and f_θ the retention curve. Equations (1) and (2) are complemented with appropriate initial and boundary conditions:

$$h = h_0 \quad \text{on} \quad \Omega, \quad t = 0 \tag{3}$$

$$h = h_D \quad \text{on} \quad \Gamma_D, \quad t \in [0, T] \tag{4}$$

$$(\boldsymbol{K} \cdot \nabla (h + z)) \cdot \boldsymbol{n} = J_N \quad \text{on} \quad \Gamma_N, \quad t \in [0, T] \tag{5}$$

with $\boldsymbol{n}$ the outward normal vector, T the simulation duration, Ω the computational domain, Γ_D the Dirichlet part of the boundary (where the value h_D is imposed) and Γ_N the Neumann part (where the flux J_N is imposed). The constitutive relations defining $\theta = f_\theta(h)$ and $\boldsymbol{K}$ have been introduced by Van Genuchten and Mualem:

$$S_e = \frac{\theta - \theta_r}{\theta_s - \theta_r} \tag{6}$$

$$S_e = (1 + |\alpha h|^\beta)^{-\nu}, \quad h < 0 \tag{7a}$$

$$S_e = 1, \quad h \geq 0 \tag{7b}$$

$$\boldsymbol{K} = \boldsymbol{K}_s S_e^{l_p} (1 - (1 - S_e^{1/\nu})^\nu)^2 \tag{8}$$

where S_e is the effective saturation, θ_r the residual volumetric water content, θ_s the saturated volumetric water content, $\boldsymbol{K}_s$ the anisotropic saturated water conductivity tensor, α a parameter related to the air entry pressure value, β a parameter related to the pore-size distribution, $\nu = 1 - 1/\beta$ and l_p the pore-connectivity parameter, usually set to 0.5.

By splitting the domain between the UZ $(h < 0)$ and the SZ $(h \geq 0)$, the following adapted θ and h-forms can be derived:

$$\frac{\partial\theta}{\partial t}=\nabla\cdot\left(\frac{\boldsymbol{K}}{C}\cdot\nabla\theta+\boldsymbol{K}\cdot\nabla z\right)+s \quad \text{in UZ} \tag{9}$$

$$S_s\frac{\partial h}{\partial t}=\nabla\cdot(\boldsymbol{K}_s\cdot\nabla(h+z))+s \quad \text{in SZ} \tag{10}$$

where $C=\partial f_\theta/\partial h$ is the capillary capacity and $S_s=C(h>0)$ is the specific storage. Equation (9) is parabolic and corresponds to a diffusion-reaction equation for θ. Equation (10) is elliptic when S_s is negligible and then corresponds to a Poisson equation for $h+z$. Both equation types are well known and efficient discretization methods exist for both of them. However, since the RE couples them in one single formulation and in the UZ the RE can become advection-dominated, the numerical solution of RE remains challenging.

Here, we modify Eq.(10) by using the false transient method to obtain a parabolic equation that can be discretized with an explicit scheme. It is done by modifying the time derivative factor as follows

$$\frac{K}{\tau}\frac{\partial h}{\partial t}=\nabla\cdot[\boldsymbol{K}\cdot\nabla(h+z)]+s \quad \text{in SZ} \tag{11}$$

where K is the largest eigenvalue of $\boldsymbol{K}$ and τ is a free parameter that controls the relaxation towards the steady state defined by Eq.(10). When the general diffusivity tensor $\boldsymbol{K}$ is simply a scaled identity matrix (i.e., for isotropic soil), it obviously reduces to K. In Eq.(11), the relaxation parameter τ can then be interpreted as the diffusivity. As such, it will constrain the stability of any explicit time discretization of that equation, i.e. as τ increases, the time step should decrease. Reciprocally, for a given time step, it is possible to determine the maximum value of τ for ensuring stability. It should be noted that the approximation of Eq.(10) by Eq.(11) is only made for numerical purposes in order to deal with a system that includes a parabolic component and an elliptic component. In the SZ, it physically amounts to increase the value of specific storage S_s.

If the h-form of Eq.(1) is used in zones where an explicit time integration scheme is stable and Eq.(11) is used otherwise, we can easily combine them as follows:

$$C_m\frac{\partial h}{\partial t}=\nabla\cdot(\boldsymbol{K}\cdot\nabla(h+z))+s \tag{12}$$

$$C_m=\max\left(C,\frac{K}{\tau}\right) \tag{13}$$

Equation (12) is exact when $C_m=C$, which is verified in most of the UZ but not in the SZ (except if $K_s/\tau\le S_s$, which is unlikely). In this case, Eq.(12) is mathematically identical to the original h-form. For practical purpose, the subset of the UZ where $C_m=C$ will be called the dry zone (DZ) and the subset where $C_m=K/\tau$ will be called the wet zone (WZ). Equation (12) works in both the UZ and SZ with an upper threshold for the diffusion coefficient equal to τ, as shown in Fig.1. Although the h-form of the equation is not mass-conservative once discretized in time, the whole algorithm is mass-conservative at the machine error precision (see Subsection 2.1 related to the mass conservation).

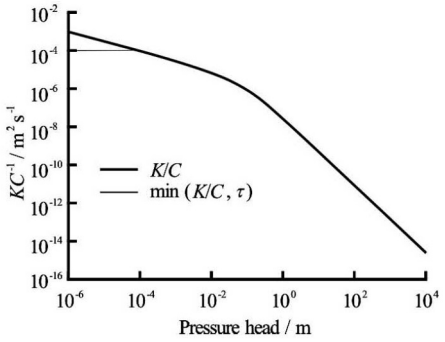

Fig.1 The effective diffusion K/C has to be limited by a threshold τ for the stability of the explicit solver

In the time-stepping algorithm described in the next section, the model equations are complemented with the following equation

$$\frac{\partial\theta}{\partial t}=\lambda\nabla^2(\theta-f_\theta(\tilde{h})) \tag{14}$$

where λ is a free parameter and $\tilde{h}$ is the value of h obtained after the time integration of Eq.(12), refreshed at each time step before the resolution of Eq.(14). Equation (14) allows us to spread out, in a mass-conservative way, the possible overshoots that can be caused by the approximation made in Eq.(13).

A weak form of the model equations is obtained by multiplying Eqs.(1), (12) and (14) respectively by the test functions u, v and $w\in H_1(\Omega)$. Taking the volume integral over the domain Ω and using the divergence theorem, we obtain the following weak formulations of RE:

$$\left\langle\frac{\partial\theta}{\partial t}u\right\rangle_\Omega=\left\langle(\boldsymbol{K}\cdot\nabla(h+z))\cdot\nabla u\right\rangle_\Omega-\left\langle\left\langle\boldsymbol{n}\cdot(\boldsymbol{K}\cdot\nabla(h+z))u\right\rangle\right\rangle_{\partial\Omega}+\left\langle su\right\rangle_\Omega \tag{15}$$

$$\left\langle C_m \frac{\partial h}{\partial t} v \right\rangle_{\Omega} = \left\langle (\boldsymbol{K} \cdot \nabla(h+z)) \cdot \nabla v \right\rangle_{\Omega} - \left\langle \left\langle \boldsymbol{n} \cdot (\boldsymbol{K} \cdot \nabla(h+z)) v \right\rangle \right\rangle_{\partial\Omega} + \left\langle sv \right\rangle_{\Omega} \tag{16}$$

which are coupled with the weak form of Eq.(14)

$$\left\langle \frac{\partial \theta}{\partial t} w \right\rangle_{\Omega} = \left\langle \lambda \nabla(\theta - f_\theta(\tilde{h})) \cdot \nabla w \right\rangle_{\Omega} - \left\langle \left\langle \boldsymbol{n} \cdot \lambda \nabla(\theta - f_\theta(\tilde{h})) w \right\rangle \right\rangle_{\partial\Omega} \tag{17}$$

where $\boldsymbol{n}$ is the outward normal vector, $<\cdot>_{\Omega}$ the volume integral over Ω and $<<\cdot>>_{\partial\Omega}$ the integral over $\partial\Omega$ the boundary of Ω.

2. Space and time discretizations

The model equations are now discretized in space by means of a discontinuous Galerkin FE scheme, and then in time with the Euler explicit time integration scheme.

2.1 *Discontinuous Galerkin space discretization*

Through partitioning the domain Ω into N non-overlapping elements Ω_e with interface Γ_e, the model variables θ and h can be approximated as

$$\theta \simeq \theta^h = \sum_{j=1}^{N_d} \theta_j \phi_j \tag{18a}$$

$$h \simeq h^h = \sum_{j=1}^{N_d} h_j \phi_j \tag{18b}$$

where N_d is the total number of degrees of freedom (DOF) and ϕ_j are piecewise polynomials defined on each element Ω_e such that

$$\phi_j(\boldsymbol{x}_i) = 1 \quad i = j \tag{19a}$$

$$\phi_j(\boldsymbol{x}_i) = 0 \quad i \neq j \tag{19b}$$

$$\sum_{j=1}^{n_e} \phi_j(\boldsymbol{x}) = 1, \quad \forall \boldsymbol{x} \in \Omega_e \tag{19c}$$

where $\boldsymbol{x}_i$ is the vector of coordinates for the node i and $n_e = N_d / N$ is the number of DOF per element. Here we use piecewise linear (P_1) basis functions for both variables. Since the discrete solution can exhibit discontinuities between mesh elements, the following jump $[\cdot]$ and averaging $\{\cdot\}$ operators on the interface Γ_e have to be introduced:

$$[x] = x^+ - x^- \tag{20a}$$

$$\{x\} = \frac{x^+ + x^-}{2} \tag{20b}$$

where the superscript "+" indicates the trace value taken on one side of Γ_e and the superscript "−" indicates the trace value on the other side, from the second element. At the boundaries, both operators are defined in terms of an external value derived from the Dirichlet boundary condition. The resulting weak boundary conditions are known to be more stable than strong ones[10,11].

The discrete equations are obtained by replacing the test functions u, v and w in Eqs.(15) and (16) by basis functions ϕ_i $(1 \le i \le N_d)$, and the solution θ and h by θ^h and h^h, respectively. Since θ^h and h^h are discontinuous between mesh elements, integration by part is performed over the partition of Ω into elements e of extent Ω_e and the interior penalty DGFEM is applied. The discrete equations thus read:

$$M_{ij} \frac{\mathrm{d}\theta_j}{\mathrm{d}t} = K_{ij} h_j + B_i + P_i, \quad 1 \le i \le N_d \tag{21}$$

$$C_{m,j} M_{ij} \frac{\mathrm{d}h_j}{\mathrm{d}t} = K_{ij} h_j + B_i + P_i, \quad 1 \le i \le N_d \tag{22}$$

$$M_{ij} \frac{\mathrm{d}\theta_j}{\mathrm{d}t} = \lambda_{ij}(\theta_j - f_\theta(\tilde{h}_j)) + P_i^\theta, \quad 1 \le i \le N_d \tag{23}$$

where $C_{m,j}$ is the C_m function evaluated at the node j, and P_i and P_i^θ are penalty terms described further,

$$M_{ij} = \left\langle \phi_i \phi_j \right\rangle \tag{24}$$

$$K_{ij} = \left\langle (\boldsymbol{K} \cdot \nabla \phi_j) \cdot \nabla \phi_i \right\rangle - \left\langle \left\langle \{(\boldsymbol{K} \cdot \nabla \phi_j) \cdot \boldsymbol{n}\} [\phi_i] \right\rangle \right\rangle \tag{25}$$

$$B_i = \left\langle (\boldsymbol{K} \cdot \boldsymbol{z}) \cdot \nabla \phi_i + s\phi_i \right\rangle - \left\langle \left\langle \{(\boldsymbol{K} \cdot \boldsymbol{z}) \cdot \boldsymbol{n}\} [\phi_i] \right\rangle \right\rangle \tag{26}$$

$$\lambda_{ij} = \left\langle \lambda \nabla \phi_i \cdot \nabla \phi_j \right\rangle - \left\langle \left\langle \{\lambda \nabla \phi_j \cdot \boldsymbol{n}\} [\phi_i] \right\rangle \right\rangle \tag{27}$$

$$\left\langle \cdot \right\rangle = \sum_{e=1}^{N} \int_{\Omega_e} \cdot \, \mathrm{d}\Omega \tag{28a}$$

$$\left\langle \left\langle \cdot \right\rangle \right\rangle = \sum_{e=1}^{N} \int_{\partial\Omega_e} \cdot \, \mathrm{d}\Gamma \tag{28b}$$

where $\partial\Omega_e$ is the contour of the element domain Ω_e. The material properties are assumed constant by element.

The DGFEM uses a piecewise linear approximation that allows discontinuities between mesh elements. The approximation however becomes continuous when the solution is smooth. Discontinuities between mesh elements usually appear when the spatial resolution is insufficient to represent sharp gradients such as the one appearing in infiltration fronts. In this case, the size of the jumps between the elements gives direct information of the local spatial error. To stabilize the diffusion term and enforce a weak continuity constraint between elements, penalty terms P_i and P_i^θ have to be added to Eqs.(21), (22) and (23)[12]. The continuity constraint on h can be expressed as

$$P_i = \sigma\left\langle\left\langle [\phi_i][h^h]\right\rangle\right\rangle \tag{29}$$

where

$$\sigma = \frac{4}{l_e}(n_0+1)(n_0+2)\boldsymbol{K}_{sc} \tag{30}$$

$$K_{sc} = \frac{(\boldsymbol{K}\cdot\boldsymbol{n})\cdot\boldsymbol{J}}{\|\boldsymbol{J}\|} \tag{31}$$

$$\boldsymbol{J} = \boldsymbol{K}\cdot\nabla(h+z) \tag{32}$$

with n_0 the order of the FE approximation (in our case $n_0=1$), K_{sc} the normal flux-oriented scalar conductivity, $\boldsymbol{J}$ the water flux, and l_e a characteristic length of the two adjacent elements. It should be noted that the exact solution for the pressure head h is continuous, while the water content θ can be discontinuous between different soil horizons. One of the advantages of DGFEM is to have the possibility to represent these discontinuities. However, imposing a continuity constraint on θ in a classical way would tend to smooth them out. The continuity constraint is thus only imposed on h with Eq.(29) to indirectly stabilize the Eq.(21). For the Eq.(23), the continuity constraint P_i^θ is expressed as

$$\boldsymbol{P}_i^\theta = \sigma_d\left\langle\left\langle [\phi_i][\theta^h - f_\theta(\tilde{h})]\right\rangle\right\rangle \tag{33}$$

where σ_d is similar to σ but with K_{sc} replaced by λ. The presence of $f_\theta(\tilde{h})$ weakly ensures similar jumps between the couples θ^{h+}/θ^{h-} and $f_\theta(\tilde{h}^+)/f_\theta(\tilde{h}^-)$. A special treatment, described in Subsection 2.5 related to the slope limiters, is needed at interfaces between media with different hydrological properties. To increase the stability, the mass matrices M_{ij} in Eqs.(21) and (22) have been lumped. Hence $C_{m,j}$ is only present on the diagonal, which allows us to avoid inverting the product $C_{m,j}M_{ij}$ at each time step. Following other model designs, we use nodal element values for $\boldsymbol{K}$.

An element is considered affiliated to the SZ, the WZ or the DZ in the following priority order: (1) if one node of the element is saturated (i.e., $h\geq 0$), the element belongs to the SZ, (2) if one node of the element has the value $C_m < C$, the element belongs to the WZ, (3) otherwise the element belongs to the DZ.

2.2 *Mass conservation*

As was mentioned above, the pure h-form of the RE is the easiest to solve but it is not mass-conservative. This is due to the time discretization of the C function which is highly nonlinear. Here we propose a simple solution to this issue based on the application of Eq.(1) as a post-processing step to achieve mass-conservation.

Using the same discretization as for Eq.(1) and an *a priori* non-conservative h-form as Eq.(12), we can yield two equations with the same right-hand side:

$$M\frac{\mathrm{d}\theta}{\mathrm{d}t} = T(h) \tag{34}$$

$$C(h)\frac{\mathrm{d}h}{\mathrm{d}t} = T(h) \tag{35}$$

where M, C, T are the matrices resulting from the spatial discretization. As M is constant in time, one could see that Eq.(34) will produce exactly-conservative results for any value of h, as the Darcy flux is included in a divergence. On this basis, we can compute an approximate solution h^* of Eq.(35) and then Eq.(34) could be solved with $T(h)\approx T(h^*)$. With such a method, mass is conserved at machine precision. The opposed approach has to be compared to models based on the classical chord-slope method[13,14], for which the mass-error decreases with the solution-error along the successive nonlinear iterations. Using an explicit iteration scheme to ensure mass conservation could theoretically be applied to any non-conservative implicit method.

2.3 *Explicit time discretization*

Equations (21) and (22) are discretized in time with an explicit Euler scheme. Using a matrix notation, the overall solution procedure is the following:

(1) Solve the equation for the intermediate steps $H^{n+1,k}$, given $H^{n+1,0} = H^n$:

For $k = 1,\ldots,m$:

$$C_m M \frac{H^* - H^{n+1,k-1}}{\frac{\Delta t}{m}} = KH^{n+1,k-1} + B + P \tag{36}$$

$$H^{n+1,k} = \lim\text{it}(H^*) \tag{37}$$

where the limiting procedure is described further in another subsection.

(2) Solve the equation for $\Theta^{n+1,0}$, given Θ^n and $H^{n+1,m}$:

$$M \frac{\Theta^* - \Theta^n}{\Delta t} = KH^{n+1,m} + B + P \tag{38}$$

$$\Theta^{n+1,0} = \lim\text{it}(\Theta^*) \tag{39}$$

(3) Compute H^{n+1} by combining $H^{n+1,m}$ and the retention curve relationship:

$$H^{n+1} = f_\theta^{-1}(\Theta^{n+1,0}) \text{ in DZ} \tag{40a}$$

$$H^{n+1} = H^{n+1,m} \text{ in WZ and SZ} \tag{40b}$$

(4) Weakly correct $\Theta^{n+1,0}$ in WZ and SZ:

For $k = 1,\ldots,q$:

$$M \frac{\Theta^{n+1,k} - \Theta^{n+1,k-1}}{\Delta t} = \Lambda[\Theta^{n+1,k-1} - f_\theta(H^{n+1})] + P^\theta \tag{41}$$

$$\Theta^{n+1} = \lim\text{it}(\Theta^{n+1,q}) \tag{42}$$

where we have replaced the reference value "$\tilde{H}$" used in Eq.(23) by H^{n+1}.

In the DZ, this algorithm reduces to the θ-form of RE. This form is known to be numerically better suited than the h-form, especially in very dry cases. In the SZ, it reduces to an approximation of the h-form which exponentially converges to Eq.(10) as m increases. The resulting approximation error leads to approximate fluxes in the SZ but the total mass is exactly conserved. Step 4 allows us to bring θ towards its correct value in both SZ and WZ.

It should be noted that when Eq.(36) has converged in the SZ, the result is equal to the one obtained with an implicit time integration scheme. Indeed, if $H^{n+1,m} = H^{n+1,m-1}$, we have reached the incompressible state which corresponds to the solution of the implicit equation for h, and also for θ once inserted in Eq.(38). To satisfy this property, the right-hand sides of Eqs.(21) and (22) have to be identical. Another point is that increasing m decreases directly the strength of the approximation. Indeed, the division of Δt by m in Eq.(36) allows us to magnify τ by a factor m.

2.4 *Selecting the values of* τ *and* λ

Any explicit time integration scheme of Eq.(21) is fully mass-conservative and valid both in the UZ and SZ but requires the field h_j to be known. Inverting the retention curve, i.e., $h = f_\theta^{-1}(\theta)$, is the easiest way to obtain it. However there is an underlying Courant-Friedrich-Lewy (CFL) stability condition. For instance, the explicit Euler time discretization reads:

$$h^n = f_\theta^{-1}(h^{n-1}) \tag{43}$$

$$\theta^{n+1} = \theta^n + \Delta t F(h^n) \tag{44}$$

where the superscripts indicate the time step, Δt represents the time step and $F(h)$ the right-hand side of Eq.(11).

One could see that this collapses exactly into the θ-form, and simple manipulations show that this is unstable when K/C is beyond the stability limit for diffusion, which is

$$\frac{K}{C} \le p \frac{\Delta l^2}{\Delta t} \tag{45}$$

where Δl is the smallest element length and $0 < p < 1$ depends on the type of explicit solver used. Although our algorithm is slightly more complex than that given by Eqs.(43) and (44), we hypothesize that its stability condition is similar and, with Eq.(13), it leads to the following condition on τ

$$\tau = \left.\frac{K(h)}{C(h)}\right|_{h=h_{\max}} \le p \frac{\Delta l^2}{\Delta t} \tag{46}$$

where $h_{\max}$ is soil-dependent.

The parameter τ controls the position of the separation between the DZ and WZ. As the solution in the WZ is approximated, it is better to limit its extent as much as possible by increasing τ. However, to respect Eq.(46) for a constant mesh size Δl, increasing τ leads to decreasing the time step. In the following, we take $p = 1/5$ in 1D case and $p = 1/15$ in 3D case.

The quasi-elliptic approximation produces fluxes in the SZ resulting in a local mass excess or deficit which has to be corrected with Eq.(41). This equation has the following stability condition

$$\lambda \le p_\theta \frac{\Delta l^2}{\Delta t} \tag{47}$$

To optimize the correction, we take the explicit diffusive limit, i.e., we take the larger stable value of λ given the sizes of the adjacent elements, in a similar way as for τ. It has been observed that a smaller value $p_\theta = 1/20$ has to be taken for stability, due to complex interactions with the UZ/SZ interface.

The present model could develop unphysical fluxes in the WZ and SZ because of the approximation in Eq.(12). The parameters p and p_θ are *a priori* fixed once for all, and τ and λ could then be fixed by the choice of Δt. The free parameters which act on the approximation are then Δt, m and q. One could easily obtain a local error of the quasi-elliptical approximation

$$e = (C_m^{n-1} - C^{n-1}) \frac{(h^n - h^{n-1})}{\frac{\Delta t}{m}} \tag{48}$$

which is exactly the flux error applied to θ at the time step $n-1$. Limiting this error below a certain threshold could then be achieved by adapting the values of m and q.

2.5 *Slope limiters*

As was mentioned previously, FE schemes can produce spurious oscillations when used with highly-variable diffusion coefficients[15]. To avoid these, we have used a technique designed for advection-dominated problems which consists in locally modifying the slope of the solution when it does not respect the monotonicity of the solution. By doing so, we aim to achieve a total variation diminishing in the mean property on each element[16]. The slope limiting algorithm used is the same as in Ref.[17]. It simply checks that the solution at the nodes of an element e is bounded by means of the solution in the neighboring elements $e_1 \dots e_{ng}$. For each mesh node j, we collect the extrema $\max_j$ and $\min_j$ of the means of all the elements including the node j. The limited value U^* of a variable U over one element e could then be expressed as:

$$U_{ej}^* = \overline{U}_e + L_e (U_{ej} - \overline{U}_e) \tag{49}$$

$$L_e = \min(1, L_e^*) \tag{50}$$

$$L_e^* = \min_{j \in e} \left(\frac{extr_{e,j} - \overline{U}_e}{U_{ej} - \overline{U}_e} \right) \tag{51}$$

$$extr_{e,j} = \max_j \quad \text{if} \quad U_{ej} - \overline{U}_e > 0 \tag{52a}$$

$$extr_{e,j} = \min_j \quad \text{if} \quad U_{ej} - \overline{U}_e < 0 \tag{52b}$$

where overlines represent the mean over one element, the indices e or j the affiliation of the variable to the element e or to the node j. This expression is correct and mass conservative only if the element has the property that the sum of its nodes weighted by their number is the mean of the element, i.e., $\sum_j U_{ej} = n_e \overline{U}_e$. All elements present in the following test cases respect this rule.

The limited values U_{ej}^* are unchanged (i.e., $L_e = 1$) if the values inside the element (i.e., $U_{ej}, \forall j \in e$) are between the maximum and the minimum of the means of their neighbors. Otherwise, the value of L_e is less than one, and the reduction in the gradients applies in all directions. It would be possible to increase the accuracy of this limiter by considering separately each spatial direction and space derivative. However, the simplicity of this algorithm has been preferred to reduce the computational cost. A 1D example is shown in Fig.2.

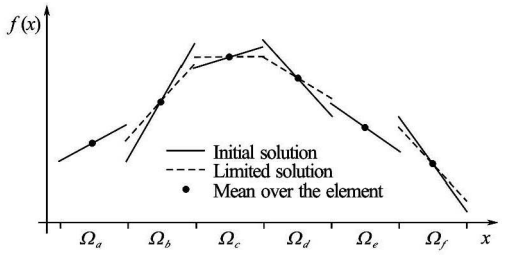

Fig.2 1D example of the slope limiter behavior. The slope of the solution on elements located at local extrema (as Ω_c) is set to zero, otherwise the solution is bounded by the means of solutions in neighboring elements, without modifying the local mass (i.e., the mean remains constant). In this example, the solution slope is limited in Ω_b, Ω_d, Ω_f but not in Ω_a and Ω_e

A different behavior is expected on the boundaries of the domain. Only tangential components to the boundary have to be limited while the normal one should not. Indeed, we want to stabilize the scheme, without limiting the extrema on the boundaries as they appear frequently in physical cases. This is achieved by using a mirror image of the solution outside of the domain.

Table 1 Modified Van Genuchten parametrization for the unsaturated infiltration test case

Sand	α (m^{-1})	β	θ_r	θ_s	θ_m	θ_k	θ_a	K_s (m/s)	K_k (m/s)
	4.1	1.964	0.02	0.35	0.35	0.2875	0.02	7.22×10^{-6}	6.95×10^{-6}

Eventually, special care must be taken for the limiter and continuity constraint applied to θ. Indeed, both have to preserve the physical discontinuities of θ between different media A and B. The way to proceed is to translate θ into h by means of the inverse of the retention curve $f_\theta^{-1}(\theta)$, as h has the property to be physically continuous. Once θ has been translated in terms of h with the properties of the medium it belongs to i.e. A or B, it is translated back into θ using the properties of the medium where the computation is necessary (resp. B or A). Then, if subscripts are used to represent the medium, one could define as

$$2[\theta^h] = (\theta_A^+ - f_{\theta_A}(f_{\theta_B}^{-1}(\theta_B^-))) + (f_{\theta_B}(f_{\theta_A}^{-1}(\theta_A^+)) - \theta_B^-) \quad (53)$$

$$\min_j^A = f_{\theta_A}\left(\min_{e \ni j}(f_{\theta_e}^{-1}(\overline{U}_e))\right) \quad (54)$$

$$\max_j^A = f_{\theta_A}\left(\max_{e \ni j}(f_{\theta_e}^{-1}(\overline{U}_e))\right) \quad (55)$$

the continuity constraint and extrema per node. The differences for the continuity constraint and the means for the limiter are then coherent with physical discontinuities of θ.

3. Numerical examples

In this section, we present three numerical examples demonstrating the ability of the model to produce results similar to the widely-used model Hydrus-1D[18], confirming its convergence as the number of iterations increase, and showing its scalability in a 3D application.

3.1 *Unsaturated infiltration*

This simulation is based on data numerically reproduced as a benchmark test in the Hydrus-1D code[18]. The experimental setup consists in a homogeneous column of soil of 0.6 m that is assumed to have an initial constant pressure head of −1.5 m. The characteristics of the soil are the same as in the Hydrus code and are represented by the modified van Genuchten-Mualem relations from Vogel and Cislerova (1988) summarized in Appendix, with the parameter values given in Table 1. The material properties are homogeneous and isotropic. At the beginning of the simulation, the pressure of a thin layer of water with the height assumed to be approximately zero is imposed at the top of the column. Mathematically, this is done by imposing the Dirichlet boundary condition $h(z=0)=0$. A zero-flux boundary condition is imposed on all the other boundaries. The spatial discretization is made with 30 equidistant layers in the vertical direction. Here, a time step of 1 s was used, with only one sub-iteration for h and θ (i.e., $m = q = 1$).

Pressure head profiles at different instants of the simulation are displayed in Fig.3. The maximum over one element remains below the means of the neighboring elements thanks to the slope-limiting algorithm. It can be seen that our results are very close to the ones obtained with Hydrus-1D[18]. In this test case, the false transient approximation does not apply. Indeed, all the elements except the top one lie in the DZ. For most natural infiltrations, dynamics happen in the DZ and are therefore not approximated.

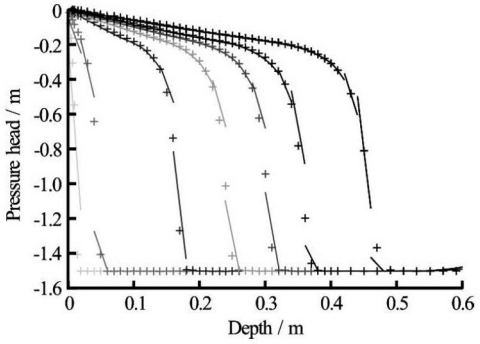

Fig.3 Pressure head profiles for an infiltration in an initially dry sandy soil at simulation times t = 1/12 min, 1 min, 15 min, 30 min, 45 min, 60 min, 90 min, from left to right. Our model results are represented by solid lines, and Hydrus-1D results by the signs "+"

The mass balance error of Hydrus at the end of the simulation is 1.95×10^{-6} m versus 2×10^{-16} m for our code (with a maximum at 6×10^{-16} m). Spatial or temporal convergence studies are difficult to fulfill with the proposed model. Indeed classical convergences orders are disrupted by the false transient approximation in the WZ and SZ, as will be shown in the next subsection. Those zones should therefore be limited to isolate proper convergences when keeping m and q constant as they are not the studied variables. Since the size of the WZ increases with the time step and decreases with the mesh size, we have to impose a maximum time step of 1 s and minimum mesh size of

0.01 m. For the mesh convergence study, the top fifth of the domain is kept fixed with a discretization of 0.02 m to make sure the WZ is always discretized with the same resolution and hence prevent the false transient approximation from interfering with the convergence analysis. Figure 4 shows a temporal convergence rate of 1 and a spatial convergence rate of 1.5. The first order explicit time integration scheme behaves as expected but it is not the case of the spatial integration scheme which is theoretically second-order accurate. Such a discrepancy is likely due to the slope limiters.

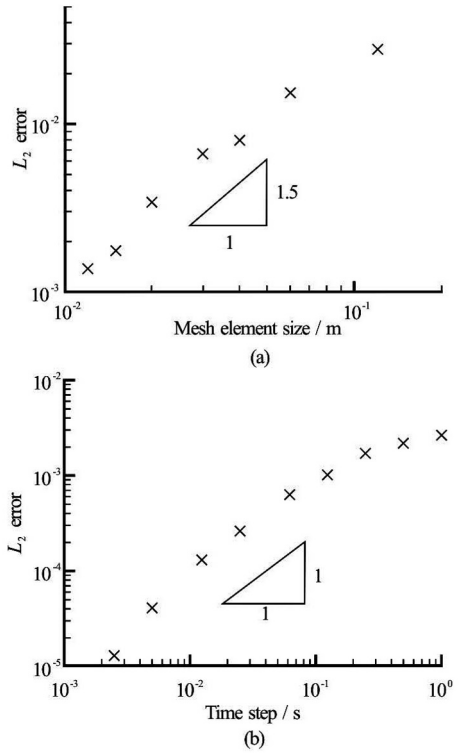

Fig.4 Mesh element size and time step convergence studies for the unsaturated infiltration test-case. The L_2 norm error is computed from the finest runs (0.01 m for the mesh element size and 1.25×10^{-3} s for the time step)

Table 2 Van Genuchten parameter values for the groundwater filling test case

	α (m^{-1})	β	θ_r	θ_s	K_s (m/s)
Sand	14.5	2.68	0.045	0.43	8.25×10^{-5}
Loam	3.60	1.56	0.078	0.43	2.89×10^{-6}
Clay	0.80	1.09	0.068	0.38	5.56×10^{-6}
Loam	3.60	1.56	0.078	0.43	2.89×10^{-6}

3.2 *Filling of groundwaters*

This second test case highlights the effects of the "quasi-elliptic" approximation in the SZ given by Eq.(11). We consider a soil of one-meter depth described by four equally-thick layers of sand, loam, clay and loam whose properties are given in Table 2. Each layer is assumed homogeneous and isotropic. Initially, the groundwater fills half of the domain and the system is at physical equilibrium. This is achieved by taking a linear initial pressure field going from 0.5 m at the bottom to –0.5 m at the top. A Neumann boundary condition is imposed at the top to represent a strong infiltration of 10^{-5} m/s that stops after 2 h. All the other boundaries are impervious. The soil column is discretized into 40 equidistant layers, the time step was equal to 1 s.

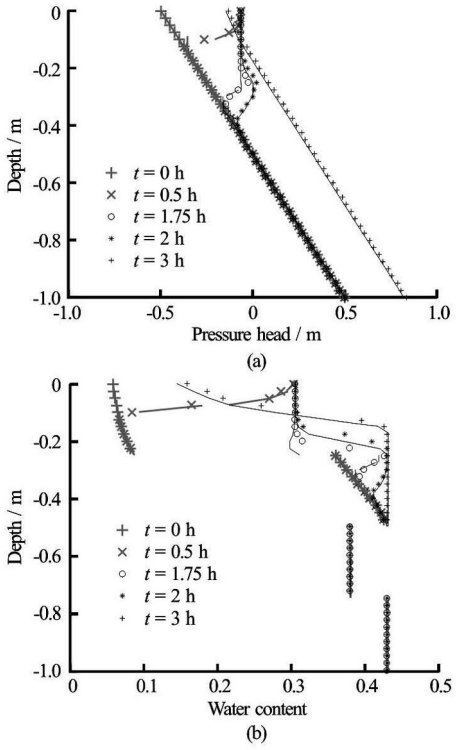

Fig.5 Infiltration profiles in a soil column initially at equilibrium. Our model results are represented by solid lines, while Hydrus-1D results are represented by the markers "+", "×", "o" and "*". Our model results are very close to those obtained with Hydrus until $t \approx 2.15$ h. Afterwards, a slight discrepancy appears due to the approximation (11)

Figure 5 shows the evolution of the h and θ profiles during the simulation. The discontinuity between different types of soils in the θ-profile is in good agreement with the physics, while a classic continuous representation would have to rely on the mean of the soil properties at the interfaces. In this model each DOF belongs to a particular material and all properties are well defined, even at the interfaces between different soil layers.

The results are similar for both models until the infiltration front reaches the groundwater depth, at around $t = 2.15$ h. Before this point, we set $m = q = 1$.

The succession of the large conductivity of the sand and the conductivity of the loam inferior to the incoming flux causes an accumulation of water at this interface. However, some of water passes through this capillary barrier and eventually fills the loam layer. Once the loam layer has been filled, the depth of the incompressible water column instantaneously increases from half to nearly 3/4 of the computational domain.

After $t = 2.15$, the h-profile is not instantaneously adapted as it should, and a curvature appears, as shown in Fig.6. This generates fluxes in the SZ leading to an increase in the water content, which is visible in the last panel of Fig.5. However, this excess is spread over time and the model converges towards the steady solution. Increasing m and q improves the convergence of the solution, as shown in Figs.6 and 7. It can be seen that a value of $m \approx 25$ is sufficient on this quick event to transport the information through 30 saturated elements.

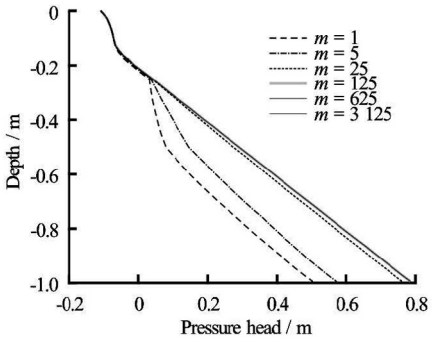

Fig.6 Pressure profile at $t = 2.2$ h. The shift results from the approximation (11), which replaces an elliptic equation by a parabolic one. This approximation converges to correct the solution as m increases. There are no visible differences for $m = 125$, 625 and 3 125

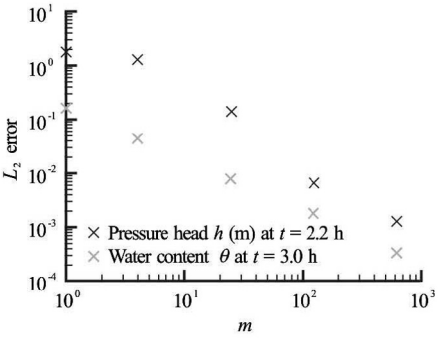

Fig.7 Error convergence computed as the L_2 norm of the difference with a solution where $m = 3\ 125$. The chosen times are such as the error is maximal

The mass balance error of Hydrus-1D at the end of the simulation is 4.78×10^{-6} m versus 5×10^{-16} m for our code (with a maximum at 10^{-15} m). For this result, the limiter on θ has been removed. It adds robustness to the algorithm but is not mandatory. The limiter applies some additional multiplications and additions to the mass variable θ, which increase the mass balance error. Despite that, with the limiter the mass balance error is not larger than 1.2×10^{-14} m.

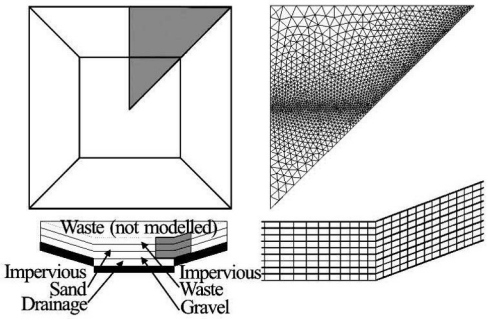

Fig.8 Top and side views of the landfill design (left) and its discretization (right). The dimensions of the pit are 5 m× 100 m×100 m, each soil layer being 0.5 m deep. The borders slope is set to 20%. The computational domain, represented in grey color in the schematic top view, is discretized into 9 layers of prisms for a total of 26 028 elements

Table 3 Van Genuchten parameters for the capillary barrier test case

	α (m^{-1})	β	θ_r	θ_s	K_s (m/s)
Waste	1.430	1.51	0.032	0.345	2.78×10^{-6}
Sand	6.340	1.53	0.046	0.345	6.57×10^{-5}
Gravel	469.0	2.57	0.074	0.419	3.50×10^{-3}

3.3 *Capillary barrier in a simple landfill design*

For this theoretical test case, a simulation of the water dynamics within the simple landfill represented in Fig.8 is considered. The waste is stocked over a capillary barrier made of sand and gravel. An impervious geotextile placed under the gravel diverts the water to the bottom where it is drained. The efficiency of the capillary barrier is assessed for an important flux of water into an initially dry system. We take advantage of the symmetries of the computational domain to model the problem only over one eighth of the domain. The waste layer is defined by soil-like properties given in Table 3 with the properties of the sand and gravel. The material properties are considered homogeneous and isotropic within each layer. The mesh is constituted of nine layers of 2 892 prisms for a total of 156 168 DOF, refined over corners as shown in Fig.8. Water input is taken as a homogeneous flux of 0.005 m/h on the top of the waste that is stopped after 12 h. The geotextile is assumed to be perfectly impervious while the drain continuously covers the bottom of the landfill. The drain boundary condition is defined as follows:

if $h < h_c$ or flux < 0 : zero flux (Neumann),

if $h \geq h_c$ and flux ≥ 0 : $h = h_c$ (Dirichlet),

where h_c is the air-entry pressure of the gravel layer. It should be mentioned that such a boundary condition is quite difficult to apply in an implicit model. Indeed, conditional statements frequently produce oscillatory states into the convergence process, as a continuous and monotone system is theoretically required to ensure convergence. The mesh used is made of prisms obtained by extruding a 2D triangular mesh. Here, we set $m = q = 1$ and use an adaptive time step which varies from 50 s at the beginning of the simulation to 0.075 s when the gravel, which is very conductive, reaches saturation. The adaptive time step algorithm simply set the time step as the minimum between 50 s and that given by the CFL condition.

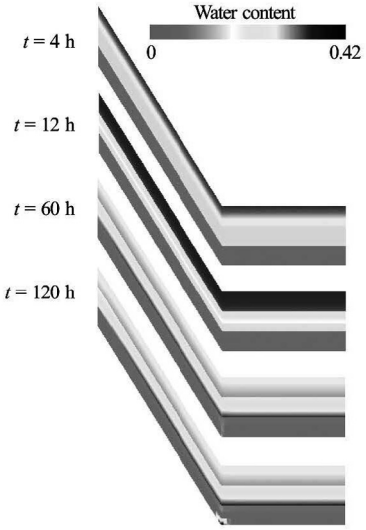

Fig.9 Clipped view of the water content in a vertical plane at the middle of the landfill domain. The infiltration in the waste ($t = 4$ h) and in the sand ($t = 12$ h) is homogeneous as expected. After one day, the water concentrates in the bottom of the sand layer, leading after 60 h to an infiltration visible at the bottom of the slope. These graphs are scaled in the vertical direction

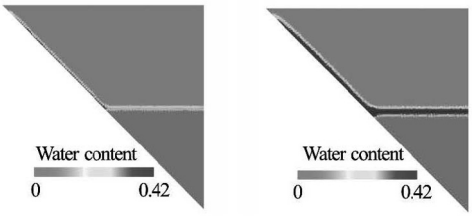

Fig.10 Bottom view of the water content in the computational domain. After 3 d, the infiltration reaches the bottom of the gravel. Then it quickly flows towards the bottom of the landfill, where it is drained

Water infiltration at the beginning of the simulation is visible on Fig.9. As expected, water crosses the capillary barrier first at the external lower corner of the domain and at the bottom of the slope, where it accumulates before being drained out, as shown on Fig.10. In the middle of the slope plane, the capillary barrier plays its role and diverts most of the water which slowly flows to the bottom of the sand layer, towards the drainage zone. The effect of the capillary barrier is also visible at the top of the corner, where a small area stays dry. On such a configuration, the most sensitive parts are the corners where the geotextile has to divert the strongest fluxes and sustains the largest water.

3.4 *Parallel efficiency*

The parallel scaling of a model is the ratio between speed-up and the number of nodes N, i.e., the fraction of available computational resources fully-used. In assessing the parallel efficiency, it is usual to distinguish between weak scaling and strong scaling. The former emphasizes the ability of a model to handle a greater computational domain with additional resources while the latter shows the scalability limit of a model for a fixed problem size. The weak scaling is the most frequently used for large-scale simulations. The ParSWMS model, on 64 nodes with 7 690 DOF per node, achieves a weak scaling of 75% in the best cases but could decrease to 29% in the worst cases as was shown in Ref.[7]. The ParFlow model has been tested for coupled surface/subsurface flows. On 100 nodes, for 2 000 DOF per node, ParFlow reaches 40% of weak scaling and for 50 000 DOF per node it reaches 72%[5]. A terrain-following grid formulation has been developed by Ref.[6] to avoid staircase boundaries. They presented a test case using 500 000 DOF per node on 16,384 nodes and achieved a weak scaling of 78% with an asymmetric preconditioner and 51% with a symmetric preconditioner. The cost per iteration is greater for the asymmetric than for the symmetric preconditioner. In the framework of DUNE, DuMu^x has achieved a strong scaling of 36% on 64 nodes with about 7 341 DOF per node. They proposed the use of an algebraic multigrid solver to overcome the bad scaling of the linear solver[9].

The first reason for the suboptimal scaling observed with all these models is the reduction of the computational domain (CD) related to each node, compared to the extent of the interfaces (I) between different CDs which require communication between nodes. A second reason is the elliptic behavior of the equation in the SZ, which implies that any change impacts the entire SZ. The information has to pass through several CDs to cover the whole SZ. It therefore requires a lot of communication (often via additional linear solver iterations). The first case could be magnified by the so-called “strong” scaling test cases, which keep the

same mesh when increasing N. Then the ratio I/CD increases and the scaling is expected to decrease. The second case is magnified by "weak" scaling test cases, which keep the sizes of the CD and the I constant when increasing N and thus the domain size as well. This results in an increase in the number of CD, which in turn increases the number of linear solver iterations and reduces the scalability. But strong scaling test cases are also affected by this situation. That is why we choose to show a strong scaling test case.

In studying strong scaling, it is important to look at the number of DOF per node, as it is closely related to the ratio I/CD. Any model will see its performances degraded below a certain ratio I/CD for which the communication time begins to dominate the overall computation time. It is then more difficult to achieve a good scaling with a small number of DOF per node. Strong scaling test cases could benefit from additional fast-memory caches as N increases, as the memory load per node decreases accordingly. This can lead to super-linear scaling.

It is conceptually difficult to develop a model of an elliptic-type equation with a perfect scaling. Mathematically, any small local change in the model solution will have a global influence. This leads to a strong exchange of information between the sub-domains linked to each computational node, and thus a poor scaling. The multigrid method is specially designed to overcome this issue. The false transient method that is used here simply reduces this exchange and thus achieves a perfect scaling by transferring information at a finite speed. The consequence that the information in an explicit method is transferred only to neighboring elements is that the number of iterations m could increase and hence reduce the efficiency as compared to implicit methods. The model efficiency would therefore be reduced in cases where the SZ occupies a large portion of the domain or is discretized with a large number of DOF's. The minimum of m in this case is of the order of $\exp(N_c)$ where N_c is the number of saturated elements in a line.

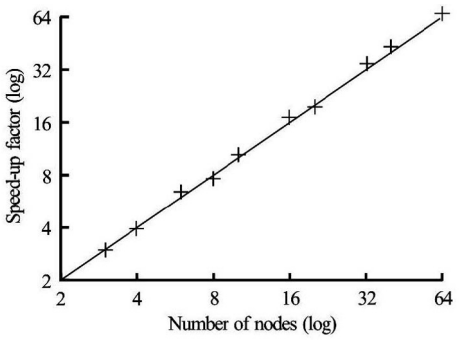

Fig.11 Scaling of the model. The line represents the theorically-expected speed-up and the signs "+" are the obtained results. It can be seen that the model scaling is optimal

The scaling of the model has been evaluated on a cluster of 64 nodes by running the model on a test-case similar to the last one, except for the 3D mesh which is now composed of 101 508 prisms, or 609 048 DOF. Speed-up results are shown in Fig.11 and exhibit an optimal scaling.

4. Conclusions

We have developed a 3D discontinuous-Galerkin model of the Richards equation using an explicit solver. As the mass variable θ is updated with the mixed-form of the equation, the mass is conserved up to machine-error precision. The DGFEM is well-suited to the advection-dominated physics that occurs at sharp gradient fronts. The DGFEM also allows the use of stabilizing techniques such as slope limiters. These limiters remove the oscillations which appear with the classical FEM. A discontinuous approximation can also nicely capture the physical discontinuities of the water content. In our model, the UZ is modeled with the θ-form of RE and the SZ by an approximation of the h-form of this equation. Such an approximation, which results in a finite pressure propagation speed, allows us to use the same explicit time integration scheme for both the saturated and unsaturated zones.

Explicit methods are constrained by a limit on the time step value, depending on the size of the elements and on the water conductivity. However, the increase in the number of time steps is balanced by a smaller computational cost per time step and an optimal scaling on parallel architectures. The latter is often hard to achieve with an implicit scheme. Explicit methods also allow a direct use of conditional statements in the resolution of the equation and in the boundary conditions, which would hamper the convergence with an implicit scheme. Eventually, the present model avoids linear or nonlinear solvers issues, and in this sense is more robust. Several codes use an explicit time integration scheme in the UZ, either because they are dedicated to this zone, or to improve the execution speed[19]. In Ref.[20], a term of the equation is set explicit to obtain a strictly convex minimization problem. To our knowledge, explicit solvers have never been used for the RE in SZ.

Accuracy and efficiency could be further improved by using a better method to solve the purely elliptic part of the equation, such as the multigrid method. Indeed, if the SZ occupies a large part of the domain, the present model could require an important number of iterations to converge. That would dramatically reduce the overall efficiency of the method. As the elliptic part is linear, a linear solver alone is sufficient, without the burden of a non-linear solver. Speed improvements could be achieved by using an interpolation for the constitutive relationships, as the power function is very time-consuming. This could be also

accomplished by using a multi-rate method, which consists in reducing the time steps only on the part of the domain where the physical processes have the smallest time scale[21]. The latter seems very promising for further developments.

Acknowledgements

De Maet T. is a research fellow with the Fonds Spécial de la Recherche (FSR) of the Université catholique de Louvain. The present study was carried out in the framework of the project taking up the challenges of multi-scale marine modelling, which is funded by the Communauté Française de Belgique under contract ARC 10/15-028 (Actions de recherche concertées) with the aim of developing and using SLIM (www.climate.be/slim). Computational resources have been provided by the supercomputing facilities of the Université catholique de Louvain (CISM/UCL) and the Consortium des Equipements de Calcul Intensif en Fédération Wallonie-Bruxelles (CECI) funded by the Fond de la Recherche Scientifique de Belgique (FRS-FNRS). The authors gratefully acknowledge Lambrechts J., De Brye B., Comblen R. and Javaux M. for their comments and help provided during the preparation of the paper.

References

[1] ZHANG Qian-fei, LAN Shou-qi and WANG Yan-ming et al. A new numerical method for groundwater flow and solute transport using velocity field[J]. **Journal of Hydrodynamics,** 2008, 20(3): 356-364.

[2] LIN Lin, YANG Jin-zhong and ZHANG Bin et al. A simplified numerical model of 3-D groundwater and solute transport at large scale area[J]. **Journal of Hydrodynamics,** 2010, 22(3): 319-328.

[3] LOTT P. A., WALKER H. F. and WOODWARD C. S. et al. An accelerated Picard method for nonlinear systems related to variably saturated flow[J]. **Advances in Water Resources,** 2012, 38: 92-101.

[4] KAVETSKI D., BINNING P. and SLOAN S. Adaptive time stepping and error control in a mass conservative numerical solution of the mixed form of Richards equation[J]. **Advances in Water Resources,** 2001, 24(6): 595-605.

[5] KOLLET S., MAXWELL R., Integrated surface-groundwater flow modeling: A free-surface overland flow boundary condition in a parallel groundwater flow model[J]. **Advances in Water Resources,** 2006, 29(7): 945-958.

[6] MAXWELL R. A terrain-following grid transform and preconditioner for parallel, large-scale, integrated hydrologic modeling[J]. **Advances in Water Resources,** 2012, 53: 109-117.

[7] HARDELAUF H., JAVAUX M. and HERBST M. et al. PARSWMS: A parallelized model for simulating three-dimensional water flow and solute transport in variably saturated soils[J]. **Vadose Zone Journal,** 2007, 6(2): 255-259.

[8] HERBST M., GOTTSCHALK S. On preconditioning for a parallel solution of the Richards equation[J]. **Computers and Geosciences,** 2008, 34(12): 1958-1963.

[9] FLEMISCH B., DARCIS M. and ERBERTSEDER K. et al. DuMux: DUNE for multi-phase, component, scale, physics,... flow and transport in porous media[J]. **Advances in Water Resources,** 2011, 34(9): 1102-1112.

[10] HANERT E., LEGAT V. How to save a bad element with weak boundary conditions[J]. **Computers and Fluids,** 2006, 35(5): 477-484.

[11] BAZILEVS Y., HUGHES T. Weak imposition of Dirichlet boundary conditions in fluid mechanics[J]. **Computers and Fluids,** 2007, 36(1): 12-26.

[12] SHAHBAZI K. An explicit expression for the penalty parameter of the interior penalty method[J]. **Journal of Computational Physics,** 2005, 205(2): 401-407.

[13] CELIA M., ZARBA R. and BOULOUTAS E. A general mass-conservative numerical solution for the unsaturated flow equation[J]. **Water Resources Research,** 1990, 26(7): 1483-1496.

[14] RATHFELDER K., ABRIOLA L. Mass conservative numerical solutions of the head-based Richards equation[J]. **Water Resources Research,** 1994, 30(9): 2579-2586.

[15] KEES C., FARTHING M. and DAWSON C. Locally conservative, stabilized finite element methods for variably saturated flow[J]. **Computer Methods in Applied Mechanics and Engineering,** 2008, 197(51-52): 4610-4625.

[16] COCKBURN B., SHU C. Runge-Kutta discontinuous Galerkin methods for convection-dominated problems[J]. **Journal of Scientific Computing,** 2001, 16(3): 173-261.

[17] AIZINGER V. A geometry independent slope limiter for the discontinuous Galerkin method[C]. **The 4th Russian-German Advanced Research Workshop.** Freiburg, Germany, 2009, 207-217.

[18] SIMUNEK J., SEJNA M. and Van GENUCHTEN M. The HYDRUS-1D software package for simulating the one-dimensional movement of water, heat, and multiple solutes in variably-saturated media[R]. University of California-Riverside Research Reports, 2005, 1-281.

[19] VANDERKWAAK J. Numerical simulation of flow and chemical transport in integrated surface-subsurface hydrologic systems[J]. **Dissertation Abstracts International Part B: Science and Engineering,** 2000, 60(7): 3170.

[20] BERNINGER H., KORNHUBER R. and SANDER O. Fast and robust numerical solution of the Richards equation in homogeneous soil[J]. **SIAM Journal on Numerical Analysis,** 2011, 49(6): 2576-2597.

[21] CONSTANTINESCU E., SANDU A. Multirate time-stepping methods for hyperbolic conservation laws[J]. **Journal of Scientific Computing,** 2007, 33(3): 239-278.

Appendix: Modified Van Genuchten-Mualem relations

Following Vogel and Cislerova (1988) the retention function and the conductivity functions are described as follows:

$$f_\theta(h) = \theta_r + (\theta_s - \theta_r)(1 + |\alpha h|^\beta)^{-\nu}, \quad h < h_s \qquad \text{(A1a)}$$

$$f_\theta(h) = \theta_s\,, \quad h \geq h_s \tag{A1b}$$

$$\boldsymbol{K} = \boldsymbol{K}_k \sqrt{\frac{\theta - \theta_r}{\theta_k - \theta_r}} \left[\frac{F(\theta_r) - F(\theta)}{F(\theta_r) - F(\theta_k)} \right]^2, \quad h \leq h_k \tag{A2a}$$

$$\boldsymbol{K} = \boldsymbol{K}_k + \frac{h - h_k}{h_s - h_k}(\boldsymbol{K}_s - \boldsymbol{K}_k)\,, \quad h_k < h < h_s \tag{A2b}$$

$$\boldsymbol{K} = \boldsymbol{K}_s\,, \quad h \geq h_s \tag{A2c}$$

with

$$F(x) = \left[1 - \left(\frac{x - \theta_a}{\theta_m - \theta_a} \right)^{1/v} \right]^v \tag{A3}$$

where θ_m, θ_a, h_k, h_s, K_k, K_s are additional empirical parameters and $\theta_s = f_\theta(h_s)$, $\theta_k = f_\theta(h_k)$.